Nano Research Energy

ISSN 2791-0091 (print); 2790-8119 (online)
https://doi.org/10.26599/NRE.2023.9120060

Research Article

Integrated radiative and evaporative cooling beyond daytime passive cooling power limit

Houze Yao, Huhu Cheng, Qihua Liao, Xuanzhang Hao, Kaixuan Zhu, Yajie Hu, and Liangti Qu (✉)

State Key Laboratory of Tribology, Department of Mechanical Engineering, Key Laboratory of Organic Optoelectronics & Molecular Engineering, Ministry of Education, Department of Chemistry, Tsinghua University, Beijing 100084, China

Received: 22 December 2022 / **Revised:** 1 February 2023 / **Accepted:** 20 February 2023

ABSTRACT

Radiative cooling technologies can passively gain lower temperature than that of ambient surroundings without consuming electricity, which has emerged as potential alternatives to traditional cooling methods. However, the limitations in daytime radiation intensity with a net cooling power of less than 150 $W \cdot m^{-2}$ have hindered progress toward commercial practicality. Here, we report an integrated radiative and evaporative chiller (IREC) based on polyacrylamide hydrogels combined with an upper layer of breathable poly(vinylidene fluoride-co-trifluoroethylene) fibers, which achieves a record high practical average daytime cooling power of 710 $W \cdot m^{-2}$. The breathable fiber layer has an average emissivity of over 76% in the atmospheric window, while reflecting 90% of visible light. This IREC possesses effective daytime radiative cooling while simultaneously ensuring evaporative cooling capability, enhancing daytime passive cooling effectively. As a result, IREC presents the practicability for both personal cooling managements and industrial auxiliary cooling applications. An IREC-based patch can assist in cooling human body by 13 °C low for a long term and biocompatible use, and IREC can maintain the temperature of industrial storage facilities such as oil tanks at room temperature even under strong sunlight irradiation. This work delivers the highest performance daytime passive cooling by simultaneous infrared radiation and water evaporation, and provides a new perspective for developing highly efficient, scalable, and affordable passive cooling strategy.

KEYWORDS

passive cooling, evaporation, radiative cooling, hydrogel

1 Introduction

Although compressor-based cooling technology is effective in achieving a reduction of object temperature, about 10% of the world's energy is consumed in this way with inconceivable levels of pollution of all kinds [1–3]. In addition, the compressor cannot reduce the overall temperature from the viewpoint of the whole environment system. Instead, it consumes electricity while transferring heat, resulting in an increase in the internal energy of the total environment and further triggering the heat island effect [1, 2]. Excessive energy consumption and significant environmental damage make scientists concentrate on seeking cleaner and more effective passive cooling methods [4].

Radiation is a heat transfer phenomenon that occurs under arbitrary spatial, temporal, and temperature conditions and is one of the most important ways to assist the earth in maintaining a relatively stable temperature in space. By effectively using the transparent atmosphere window of 8–13 μm, objects on the surface of about 300 K can efficiently emit heat to outer space without consuming energy or emitting pollutants based on Planck's blackbody radiation law. In 2014, scientists proposed a selective emission surface realized by a photonic crystal structure of quartz/SiC, and further prepared a high infrared emission surface with low visible light absorption by SiO_2/HfO_2 [5], and established a truly all-weather radiative cooling system [6]. In the following years, materials based on photonic crystals, metasurfaces, and molecular design have been reported to achieve selective atmospheric window thermal radiation and excellent cooling effect [7–11]. In particular, polymer materials, such as cellulose, polyvinylidene fluoride [12], polyethylene [13], polyethylene oxide [14], polydimethylsiloxane [15], poly(methyl methacrylate) [16], etc., have attracted a large number of researchers' attention due to their inherent infrared selective emission, which can achieve large area daytime passive radiative cooling at low cost by simple microstructural adjustments.

However, as predicted by Planck's blackbody radiation law [17–19], the theoretical net radiative cooling power of an object with a temperature of about 300 K cannot surpass 150 $W \cdot m^{-2}$. Although some work has proposed combining radiative cooling materials with hygroscopic materials that absorb surrounding water at night to augment daytime heat dissipation [20, 21], no

Address correspondence to lqu@mail.tsinghua.edu.cn

substantial progress has been seen with only about 100 W·m^{-2} improvements in cooling power at ambient temperature. Moreover, the cooling mode based on absorption and desorption limits the application environment and is severely restricted by the water vapor diffusion process after scaling up. As a result, radiative cooling materials are still not able to meet the cooling needs in practical applications.

Here, we propose a novel concept of integrated radiative and evaporative cooling technology of simultaneous passive heat dissipation through infrared radiation and persistent water evaporation, which achieves uninterrupted cooling and breaks the power limit of daytime passive cooling (Fig. 1(a)) [22–27]. An integrated radiative and evaporative chiller (IREC) is fabricated and achieves a record-high net cooling power of more than 710 W·m^{-2} during daytime. In addition, the continuous water flow is sufficiently robust to support long periods of outdoor passive cooling. Water as a work mass carries the cold energy, providing a broader prospect of cooling applications.

For the radiative and evaporative cooling system (Fig. 1(b)), the net cooling power $P_{cooling}$ can be defined as

$$P_{cooling} = P_{evap} + P_{rad} - P_{atm} - P_{solar} \quad (1)$$

where P_{evap} is the evaporative cooling power, P_{rad} is the radiative power on the surface, P_{atm} is the total power gained from the atmosphere in the form of heat convection, heat radiation, and heat transfer, and P_{solar} is the power gained from solar irradiation, respectively. IREC is fabricated based on porous polyacrylamide (PAM) hydrogels covered with breathable poly(vinylidene fluoride-co-trifluoroethylene) (P(VDF-TrFE)) fibers (Fig. 1(c)). By introducing the reflective layer, P_{solar} is effectively reduced while P_{rad} is increased. Fibers with a diameter close to the wavelength of visible light provide a visible light reflectivity of more than 90% at a much wider incident angle range of −85° to +85°, and an excellent emissivity of more than 76% under an atmospheric window. The intrinsic sunlight absorption by the water used for evaporative cooling is avoided based on a reasonable pro-hydrophobic design of the radiative cooling layer. As a result, the composite hydrogel, which effectively reduces the energy input from sunlight and improves the net cooling power during the daytime without decreasing the evaporation rate, can be applied as the IREC. In addition, forced fluid heat transfer is applied to capture cold energy more efficiently owing to the water permeability of porous hydrogels. This unique integrated design effectively increases passive cooling power during the day and offers a potential active cooling mode, significantly broadening the scope of applications for this technique.

2 Experimental section

2.1 Materials

P(VDF-TrFE) powder (70 mol.%/30 mol.%, M_w = 1.5 × 10^4, Piezotech, France), polyacrylonitrile (PAN) powder (M_w = 1.5 × 10^4, Innochem), dimethylformamide (DMF) (Innochem), acetone, (Beijing Tongguang fine chemicals company), acrylic amide (Greagent), N,N'-methylenebisacrylamide (MBAA) (Adamas), tetramethylethylenediamine (TEMED) (Macklin), ammonium persulphate (APS) (Macklin), 3-(trimethoxysilyl)propyl methacrylate (TMSPMA) (Alfa). Anti-fever patches were bought from Kobayashi Pharmaceutical Co. Ltd., Sunflower Pharmaceutical Co. Ltd., and Kokubo & Co., Ltd.

2.2 Preparation of P(VDF-TrFE)-PAN nanofiber nonwovens

P(VDF-TrFE) powder was dissolved in a mixture of DMF and acetone (3:2, mass ratio) at 60 °C to prepare the P(VDF-TrFE)

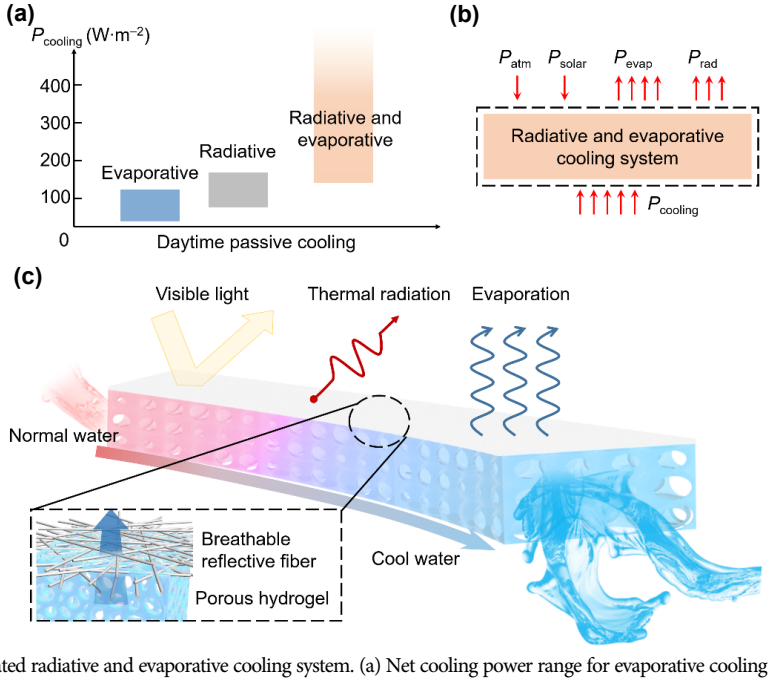

Figure 1 Schematic of the integrated radiative and evaporative cooling system. (a) Net cooling power range for evaporative cooling systems, radiative cooling systems, and integrated radiative and evaporative cooling system during the daytime. (b) Energy balance applied to the radiative and evaporative cooling system (dashed line). When the sample is in equilibrium, the net flux is zero and determined by the two outgoing fluxes from the emission of the sample (P_{rad}) and the evaporation (P_{evap}), and the three incoming fluxes from the total power gained from the atmosphere (P_{atm}), input solar energy (P_{solar}) and the net cooling power ($P_{cooling}$). (c) Functional structure of the hydrogel for IREC. The composite hydrogel is polymerized at sub-zero temperature to obtain a porous water transfer channel with a permeable reflective fiber layer modified on the surface. Through the evaporation of water, radiation of fibers and reflection of visible light, IREC can effectively cool the free water flowing in the hydrogel during the day.

solution (10%, mass ratio). PAN powder was dissolved in DMF at 100 °C to prepare the PAN solution (10%, mass ratio). After dissolved, and stirred for 12 h, the polymer was completely dispersed in the solvent. The electrospinning of the two solutions used the same experimental parameters as follows: voltage 20 kV, receiving distance 20 cm, propulsion speed 1.4 mL·h^{-1}, needle inner diameter 0.4 mm (#22G), receiver speed 100 r·min^{-1}. The obtained nonwovens were then dried in a vacuum oven at 60 °C for 5 h.

2.3 Preparation of porous PAM hydrogel

The mass ratio of monomer Acrylamide (AM) and crosslinker MBAA was 10:1. APS and TEMED were initiators, accounting for 0.83 wt.% of the polymer precursor, respectively. In this work, we used a 4% precursor solution to prepare PAM hydrogel. Typically, 10 g AM, 1 g MBAA, and 0.09 g TEMED were dissolved in 11 g deionized (DI) water to prepare a 50% concentration precursor solution. Then, 8 g of this solution was diluted to 100 g DI water and then was refrigerated to 4 °C. After adding 330 μL of APS solution (10%), the mixed solution was quickly transferred to the mold and reacted at −11 °C for 12 h. Subsequently, the prepared frozen hydrogel was slowly thawed in ethanol. Finally, the hydrogel was soaked in DI water 12 h for three times to remove possible residual monomers.

2.4 Preparation of IREC

It is similar to the method of preparing PAM hydrogel, except that the precursor solution was transferred to the PAN layer of the nonwovens obtained by electrospinning.

2.5 Fabrication of IREC adhesive tape

An example of making IREC on aluminum tape. The experimental parameters were referred to previous studies [28, 29]. After the aluminum tape was cleaned and dried by ethanol, it was treated under plasma for 5 min to make the surface with oxygen-containing functional groups. Subsequently, the aluminum surface was treated with a 1% TMSPMA aqueous solution for 1 h, and then washed with ethanol and DI water three times and then dried. A homemade mold is used, a non-woven fabric and aluminum tape were clamped on the front and back sides of the container. Then, the precursor solution was added in and contacted with both surfaces at the same time, followed by polymerization at −11 °C.

2.6 Characterization and measurements

The morphological structures were characterized by scanning electron microscopy (Gemini 300). Thermogravimetric analysis was performed by using a thermogravimetric analyzer (TGA/DSC, STA449F3) under air, and the heating rate was 10 K·min^{-1}. The temperature was measured by thermocouples with multi-channel temperature tester (AT-4516). The optical transmittance and reflectance spectra of the IREC were measured on a varian ultraviolet–visible (UV–vis) spectrophotometer (Cary 7000) with an Agilent integrating sphere. The infrared emissivity was measured by an infrared microscope (Bruker). The solar intensity was measured by a reference cell and meter (91150V, Newport). The outdoor solar flux was measured through a pyranometor (RS-RA-N01-AL, Shandong Renke Control Technology Co., Ltd.). The thermostat was custom made at Anthone Electronice Co., Ltd. The power of the heater was recorded by means of an electric power meter (PM9800, Napui). All weights were measured by analytical balance (METTLER TOLEDO ME104E).

2.7 Radiative and evaporative cooling performance experiment

In the homemade 10 cm × 10 cm mold, the water flow was realized through the silicone tube connected to the peristaltic pump. The outside of the mold was insulated with 2 cm thick thermal insulation foam, which had an aluminum foil cover to reduce the influence of light. The silicone tube with an inner diameter of 5 mm was also wrapped by an insulating cloth to reduce possible heat effects. Thermocouples were inserted in the water input and output to measure the temperature change of the water body in real-time. The solar simulator was adjusted to the light intensity of 1000 W·m^{-2}. Then, a shading plate was applied to control the irradiation area equal to the container area. Finally, IREC was directly placed in the mold with the water flow start.

The experimental process in outdoor environment is basically the same. The raw water used was sealed and placed in the air to make its temperature close to the air temperature. The solar flux was measured by a pyranometor and its value corresponded to the Global Horizontal Irradiance.

2.8 Static radiative and evaporative cooling performance experiment

A 10 cm × 10 cm electric heating sheet with a heating power of 10 W (1000 W·m^{-2}) was placed on the insulation layer and connected to the copper sheet through heat-conductive silicone, and thermocouples were soldered to the copper sheet. Subsequently, the wetted IREC was placed on the copper sheet. A negative feedback thermostat adjusted the heating process of the heater by monitoring the air temperature to equal the measured IREC temperature to the air temperature. The output power of the electric heater was recorded using an electric power meter.

2.9 Experiment of IREC preventing the container from insolation heating up

In a 10 cm × 10 cm × 5 cm stainless steel square box, 300 mL of ethylene glycol was added as the liquid to be measured. Various materials were employed to decorate the top cover of the container, such as directly pasting the IREC tape on the upper surface. Subsequently, the container was placed under the solar simulator, and the irradiated area was controlled to be equal to the area of the container through a shading plate. The temperature of the oil was measured in real-time by a thermocouple.

2.10 The simulated auxiliary cooling test of dry IREC

A 2.8 cm × 5 cm electric heater was set up as a heat source to simulate the heating of the human body. The heating power was adjusted to 450 W·m^{-2} through the direction current (DC) power supply (2 V, 0.31 A). At this time, the surface temperature of the electric heating plate was stably maintained at 37.5 °C. IREC was placed directly on the electric heating plate, and a peristaltic pump was used to feed water to simulate the outflow of sweat. A thermocouple was used to measure the temperature of the electric heating plate in real-time.

2.11 The simulated auxiliary cooling test of IREC

A 2.8 cm × 5 cm electric heater was used as a heat source to simulate the heating of the human body. The heating power was

adjusted to 450 W·m^{-2} through the DC power supply (2 V, 0.31 A). IREC was pre-soaked in water and then placed directly on the electric heating plate. When the temperature of the electric heating plate was higher than 35 °C, it was considered that all the water in the IREC had evaporated. Then the IREC was taken out, and the experiment was repeated again after IREC was soaked in water for 10 minutes. The IREC was placed on the human skin surface in a similar way and a thermocouple was used to measure the skin surface temperature. Written informed consent had been collected from all participants who using IREC.

3 Results and discussion

3.1 Design principle and fabrication of IREC

The IREC is prepared in a large scale by a roll-to-roll electrospinning process and a solution gel method (Fig. 2(a)). In order to ensure a good combination of the hydrogel and the nonwovens, P(VDF-TrFE) and PAN are first used to form a heterogeneous film by electrostatic spinning (Fig. 2(b)). Scanning electron microscope (SEM) images show the uniform entanglement of the two kinds of fibers into a film (Figs. 2(b) and 2(c)). The mapping images of F and N elements from the energy dispersive spectrometer (EDS) show the distribution of P(VDF-TrFE) and PAN (Fig. 2(d)). The upper layer of P(VDF-TrFE) has a 134° contact angle of hydrophobicity, while the lower layer of PAN can absorb all the droplets through capillary force (Figs. 2(e) and 2(f)). Therefore, the precursor solution of the hydrogel can be filled into the PAN layer and part of the P(VDF-TrFE) layer from the PAN side to obtain good interfacial bonding. After optimization, the thickness of P(VDF-TrFE) is about 200 μm and the thickness of PAN is about 100 μm in the composite nonwoven. The increase of P(VDF-TrFE) layer thickness will lead to the decrease of air permeability. The whiteness of the surface features a strong scattering of visible light, which is attributed to the multilayer structure of randomly stacked nanofibers with a wide distribution of diameters and sizes (centered at ~ 527 nm, Fig. 2(g)). By inducing the formation of ice crystals in the precursor solution during low-temperature polymerization (see details in methods), a hydrogel structure with inter-perforation can be obtained, and the pore diameter is about 50–200 μm (Fig. 2(h)). The enlarged SEM image shows the structure of the fibers interspersed in the polymer, which further confirms a strong bond between the hydrogel and the nonwovens (Fig. 2(i)). Besides, the wettability gradient of the heterogeneous film leads to the filling of PAM in part of P(VDF-TrFE), resulting in a thickness thinning of the exposed fiber layer (Fig. S1 in the in the Electronic Supplementary Material (ESM)). This design makes it impossible

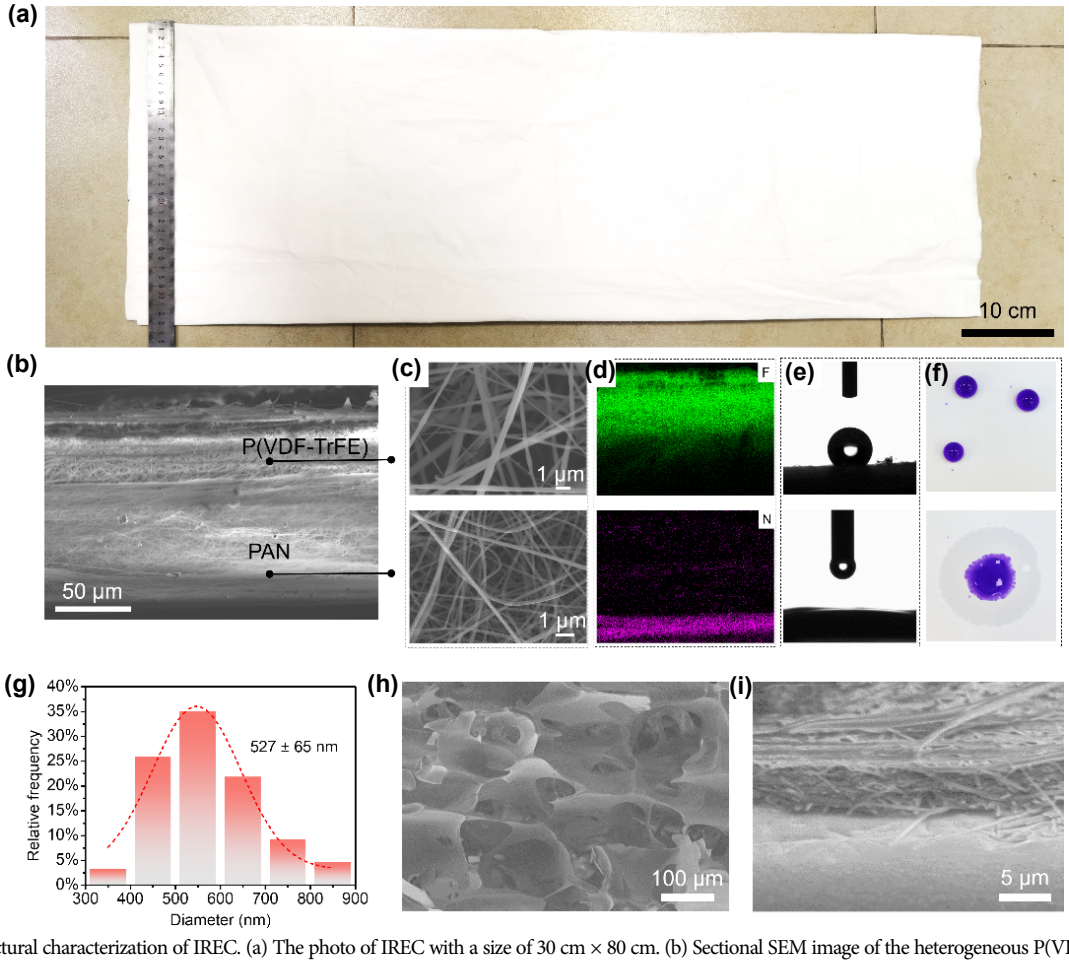

Figure 2 Structural characterization of IREC. (a) The photo of IREC with a size of 30 cm × 80 cm. (b) Sectional SEM image of the heterogeneous P(VDF-TrFE)/PAN nonwovens. (c) SEM images of the P(VDF-TrFE) fiber and PAN fiber, respectively. (d) EDS images of sectional nonwovens with corresponding elemental mapping images of F, and N, respectively. F element and N element are the characteristic element of P(VDF-TrFE) and PAN, respectively. (e) P(VDF-TrFE) nonwovens exhibited a water contact angle of 134°, while PAN nonwovens can absorb droplets into the membrane. (f) Photographs of dyed droplets on the surface of polyvinylidene fluoride (PVDF) and PAN fibers. (g) The histogram of the statistical distribution of P(VDF-TrFE) fiber diameter, and the fiber diameter is 527 ± 65 nm. (h) SEM image of porous channels in PAM hydrogel. (i) SEM image of PAM filled in fiber layer. PAM selectively fills in the hydrophilic side of the P(VDF-TrFE)/PAN nonwovens.

for water to pass through the fiber layer as a liquid at normal pressure, but only as a gas (Fig. S2 in the ESM). AM is selected as the monomer, and the freezing point of AM solution with different concentrations is measured by differential scanning calorimetry test (Fig. S3 in the ESM). As the temperature of AM solution decreased, two crystallization behaviors appeared, which represented the formation of ice crystals and the solidification of the mixed-phase, respectively (Fig. S4 in the ESM). By adjusting the concentration of AM solution, the porosity of PAM hydrogel can be continuously adjusted (Fig. S5 in the ESM). AM solution with a mass fraction of 4% is chosen, and the corresponding porosity of PAM is 85%. This porous hydrogel structure can not only quickly discharge the free water in the pores during squeezing (Figs. S6 and S7 in the ESM), but also has a fast water transport ability (Fig. S8 in the ESM). The good water transportability design in IREC lays the foundation for continuous water cooling and reuse.

3.2 Radiative and evaporative cooling performance of IREC

As predicted by Mie's theory [30, 31], the surface of IREC has a strong scattering effect on visible light, with a statistical average reflectance of over 90% in the 500–2000 nm range (Fig. 3(a)). Meanwhile, since there are only C–C, C–H, and C–F vibrations in the P(VDF-TrFE), the surface of IREC exhibits desirable selective infrared emission, with an emissivity of 76% on average in the atmospheric window (Fig. 3(b)). Strong scattering of visible light is observed due to the size of the fibers is comparable to the visible wavelength. And as a result, IREC maintains a reflectivity of up to 90% even at a wide incident angle range of ±85° (Fig. 3(c) and Fig. S9 in the ESM), ideal for all-day and all-region radiative cooling. The cooling ability of IREC is further analyzed through the indoor water evaporation performance [32, 33]. In the absence of light, the water evaporation rate (WER) of IREC is about 0.46 kg·m^{-2}·h^{-1}, which is close to the WER of PAM hydrogel of 0.49 kg·m^{-2}·h^{-1} and twice as high as that of bulk water, indicating that the porous PAM hydrogel can accelerate the natural evaporation of water (Fig. 3(d)). The addition of the P(VDF-TrFE)/PAN nonwovens do not hinder the transmission of vapour, which is relevant to its actual covering thickness of 10 μm. Under 1 sun irradiation (1 kW·m^{-2}), the WER of both the bulk water and the hydrogel increased significantly, reaching 0.56 and 1.13 kg·m^{-2}·h^{-1} respectively. However, the WER of IREC increased only slightly, from 0.46 to 0.58 kg·m^{-2}·h^{-1}, indicating that IREC successfully scattered most of the incident light (Fig. 3(e)). It is worth noting that since both bulk water and hydrogel are visible light permeable, the bottom light absorption capability significantly affects the evaporation rate, and thus a black underlayer is chosen (Fig. S10 in the ESM). While the evaporation rate of the IREC is independent of the chosen substrate. The source of energy consumed for evaporation is related to the light intensity and the temperature of sample (Note S1 in the ESM). By measuring the sample temperature and the water evaporation rate (Fig. S11 in the ESM), the source of energy consumed by water evaporation can be determined [34–37]. Compared to the evaporation process of water and PAM hydrogel, IREC reflects more incident light, and about 69.2% of the heat consumed in the evaporation process is gained from the environment under 1 sun irradiation (Fig. 3(f)). This further implies that IREC is selectively dedicated to cooling the environment with evaporation.

Simulated light experiments verified this strong cooling ability of IREC under light. A set of adiabatic device systems based on a solar simulator that can flow water has been first established (Fig. S12 in the ESM). The container with IREC is wrapped by insulation foam, and the area available for water flow and evaporation is 10 cm × 10 cm. A peristaltic pump is used to adjust the flow rate of water in IREC. A thermocouple is placed at the inlet and outlet to detect the water temperature. The light intensity of the solar simulator in the experiment is 1 kW·m^{-2}. As the water body evaporates continuously in IREC, the low heat transfer coefficient causes the water body temperature to decrease continuously, and the outlet water temperature can be reduced by up to 7 °C with a temperature drop gradient of more than 0.7 °C·cm^{-1} under room temperature. In contrast, the temperature is almost no change when only using hydrogel system and will increase when only based on bulk water. This result further confirms the rationality of introducing the reflective nonwovens in IREC.

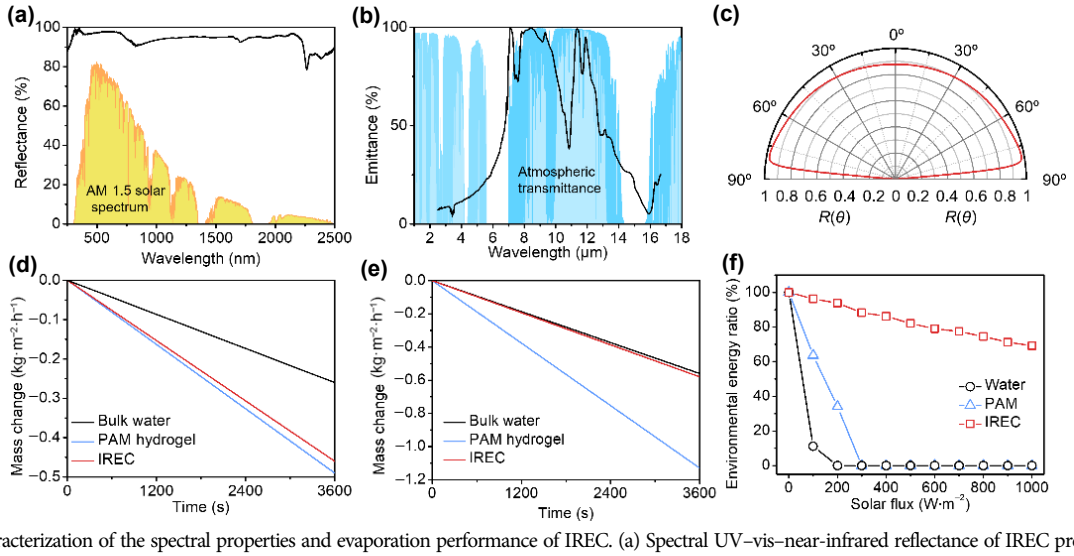

Figure 3 Characterization of the spectral properties and evaporation performance of IREC. (a) Spectral UV–vis–near-infrared reflectance of IREC presented against the AM1.5 solar spectra. (b) Spectral infrared emittance of IREC presented against the atmospheric transparency window. (c) Polar distribution of the average reflectance across the visible light of the IREC at different incident angles (θ) from 0° to 90°. (d) The mass change of bulk water, PAM hydrogel, and IREC under dark conditions. (e) The mass change of bulk water, PAM hydrogel, and IREC under 1 sun irradiation. (f) The ratio of energy consumed from the environment by bulk water, PAM hydrogel, and IREC when evaporated under different solar flux, respectively.

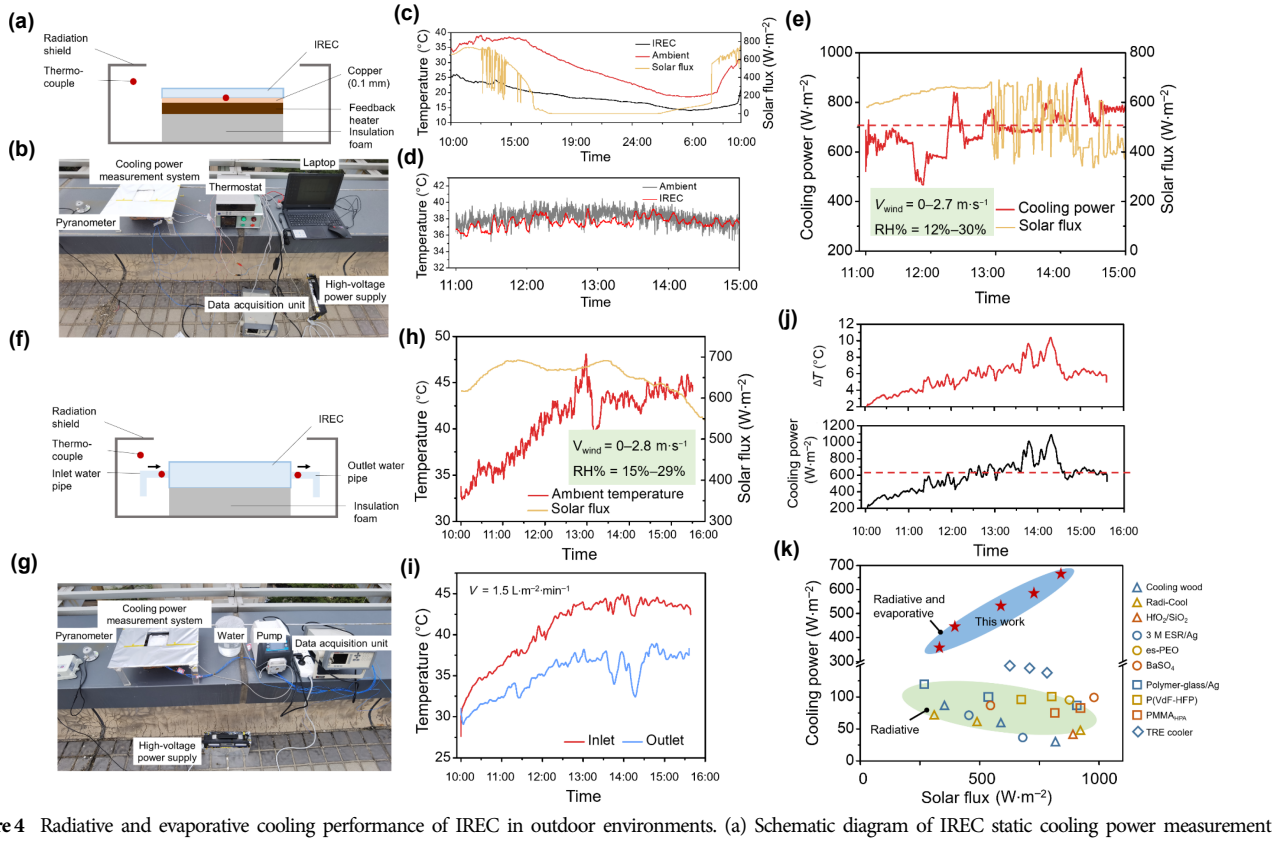

Figure 4 Radiative and evaporative cooling performance of IREC in outdoor environments. (a) Schematic diagram of IREC static cooling power measurement system. (b) Photo of IREC static cooling power measurement system. (c) Solar flux, temperatures of the air and IREC without the use of a heating system. The experiment run in Beijing from May 16 to 17, 2022. (d) Red curve is the temperature of IREC with thermal compensation. The gray background curve is the air temperature. (e) Real-time solar flux and equivalent cooling power during testing. The average cooling power is 710 W·m^{-2}. Wind speed and humidity are marked in the figure. The outdoor experiment was carried out on July 8, 2022 in Beijing. (f) Schematic diagram of IREC cooling power measurement system under water flow. (g) Photo of the cooling power measurement system with water flow applied by pump. (h) Real-time solar flux and ambient temperature during testing. The outdoor experiment was carried out on July 7, 2022 in Beijing. (i) Temperature at the inlet and outlet. Inlet water temperatures are controlled to be close to ambient air temperature. (j) The temperature difference between inlet and outlet and the calculated cooling power. (k) Comparison of the passive cooling power of various passive cooling methods under different solar flux.

An outdoor cooling performance measurement system was further established to measure the cooling power of IREC under static evaporation (Fig. 4(a)). A negative feedback heating system makes the temperature of the IREC equal to the atmospheric temperature and thus calculates the cooling power of the IREC (Fig. 4(b)). Without the heating system enabled, IREC produced a maximum temperature difference of 14 and 7 °C from the air ambient during the day with a solar flux of 700 W·m^{-2} and night with no solar irradiance, respectively (Fig. 4(c)). The static radiative and evaporating cooling effect test was conducted outdoors in Beijing on July 8, 2022. A heating system detects air temperature changes in real time and heats the IREC to the same temperature as the air (Fig. 4(d)). The average cooling power during the day is about 710 W·m^{-2} (Fig. 4(e)), which has never been achieved as far as we know for passive daytime cooling. Even under cloudy conditions with a low solar flux, the average net cooling power outdoors can still be 300–500 W·m^{-2} (Fig. S13 in the ESM). The drop in performance comes from the fact that radiation is hindered by clouds and evaporation is inhibited under high humidity. We also compared the individual cooling effect of radiative cooling, evaporative cooling with IREC (Fig. S14 in the ESM). The single use of radiative cooling and evaporative cooling power is about 65 and 200 W·m^{-2} respectively, while the integrated radiative and evaporative cooling power up to 650 W·m^{-2}. The cooling power of IREC is much greater than the sum of radiative and evaporative cooling power used separately. This enhanced cooling effect stems from the effective solar energy shielding of the radiative cooling layer, further validating the rationality of our design. IREC was further applied to cool the flowing water body to characterize its cooling capacity in practical cooling applications (Fig. 4(f)). The outdoor flow cooling tests demonstrated the great potential of IREC for working mass cooling (Fig. 4(g)). By measuring the flow rate and temperature change of the water, the cooling power $P_{cooling}$ that IREC actually cools the water can be easily calculated by Eq. (2)

$$P_{cooling} = (T_1 - T_2)\,VS \tag{2}$$

where T_1 and T_2 are the temperature of input and output water, respectively, V is the flow rate of water and S is the specific heat capacity of water. The temperature drop of the water can be changed by adjusting the variation of the flow rate [38], thus giving the optimum actual cooling power (Fig. S15 in the ESM). Raising the flow rate makes the temperature difference decrease, which helps to reduce the heat exchange with the environment, leading to an increase in net cooling power. This process was modeled and analyzed using COMSOL [39, 40] to confirm the mechanism that flow rate affects internal heat transfer and external heat loss (Fig. S16 and Note S2 in the ESM). Detailed temperature measurements of multiple locations inside the IREC were detected through thermocouples, and the temperature change process was essentially the same as the simulation (Fig. S17 in the ESM). When using an optimal flow rate of 1.5 L·m^{-2}·min^{-1},

the inlet and outlet maintain a temperature difference of 6.0 °C and the net cooling power can reach 630 W·m^{-2} (Figs. 4(h)–4(j)). The sharp temperature fluctuations in the data are caused by sudden gusts. We have avoided this effect in the calculation of the average cooling power. Our experiments have shown that the actual cooling capacity of IREC can reach 350–630 W·m^{-2}, depending on environmental fluctuations (Fig. S15 in the ESM). The high cooling power capacity makes the energy consumption of the pumping system (< 10 W·m^{-2}) negligible. Compared with the report of the passive cooling system, the IREC we developed here has made a significant breakthrough in passive cooling performance [5, 7–9, 12, 14, 22–25, 41] (Fig. 4(k)).

3.3 Application of IREC

IREC can be directly employed to assist the human body to quickly dissipate heat and cool down, imitating the way the human body sweats to cool (Figs. 5(a) and 5(b)). We first tested the cooling effect of IREC in the dry state under different amounts of sweat. A heating plate with a constant temperature of 37.5 °C is used to simulate the surface of the human body [42–44], and the power density is about 450 W·m^{-2}. A peristaltic pump is deployed for water supply to simulate the secretion of sweat. The amount of human sweat fluctuates greatly according to different parts and health status, and can exceed 1000 g·m^{-2}·h^{-1} in the most intense exercise [45–47]. IREC can quickly absorb sweat and evaporate *in situ*, resulting in a significant cooling effect on the contact surface (Fig. 5(c)), which proves that IREC can assist the human body in perspiration and heat dissipation. In addition, for non-exercise human fever, IREC in the wet state can assist in cooling the heat-producing parts of the human body for a long time after actual testing on human skin. Both the cooling effect and service time are better than that of commercial anti-fever patches (Fig. 5(d)). After the water in IREC has evaporated, IREC can be soaked in water to recover for reuse (Fig. 5(e)). Besides, IREC has excellent properties of rollable, foldable, and twistable and is easy to apply on human skin (Fig. 5(f)). The flexibility of the IREC allows for washing and wiping under a stream of water and even under mechanical stirring (Videos S1 and S2 in the ESM). And the reflectivity of the surface does not change after thirty times of washing (Fig. S18 in the ESM). Compared with a variety of commercial anti-fever

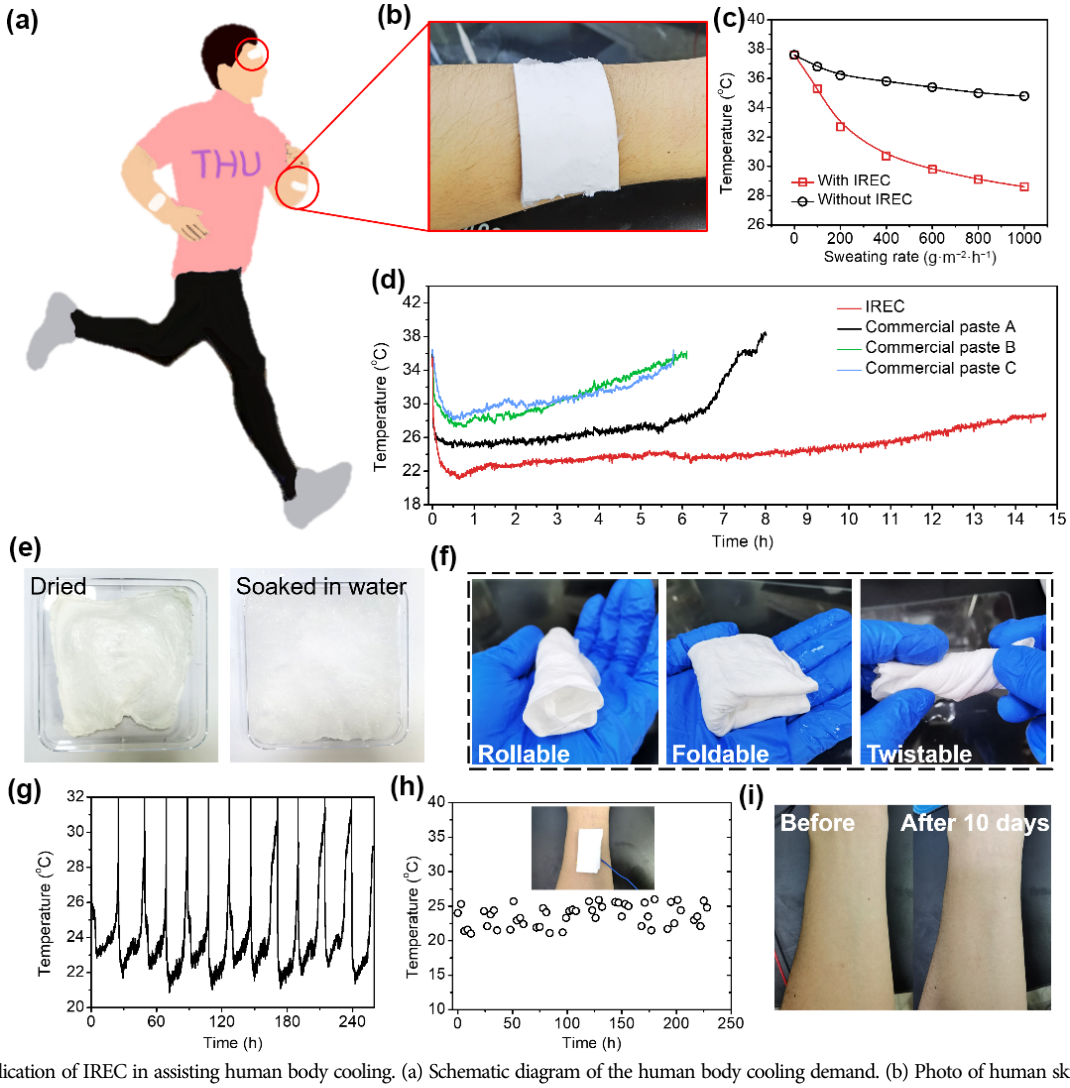

Figure 5 Application of IREC in assisting human body cooling. (a) Schematic diagram of the human body cooling demand. (b) Photo of human skin surface using IREC to dissipate heat. (c) The simulated skin temperature with and without IREC under different sweating rates. (d) The simulated skin temperature with IREC and commercial anti-fever pastes of different brands. (e) Photos of dried IREC and the restored IREC after submersion in water. (f) Photos of IREC show that IREC is rollable, foldable, and twistable. (g) The continuous auxiliary heat dissipation test of IREC. IREC is put in the water for 10 min when dried and then continued the test. (h) A cyclical test using IREC to cool human skin. The temperature is measured every 3 h in daytime, and the IREC are soaked in water for 10 min every 12 h. (i) Photos of the skin before and after 12 h of continuous daily use of IREC for 10 days.

patches, IREC has a continuous operating time of more than 12 h, and can be reused more than ten times (Fig. 5(g)). Further continuous use on human arm skin showed that IREC maintained good cooling performance even after 10 days of cycling, demonstrating stability for long-term application (Fig. 5(h)). Since only water is involved as the cooling agent, no irritation to human skin is observed (Fig. 5(i)). Based on the high outdoor cooling power and excellent indoor cooling effect, IREC is expected to be applied for efficient human cooling in outdoor conditions.

To further prove the strong compatibility and wide usability of IREC, a homemade mold is used to prepare IREC on metal-based adhesive tape. By modifying 3-(trimethoxysilyl)propyl methacrylate on the surface of metal foil such as aluminum, the hydrogel layer of IREC can be firmly bonded to the metal-based adhesive tape through covalent cross-linking [28, 29] (Fig. 6(a)–6(c)). This aluminum tape with an integrated radiative and evaporative cooling function can be applied to the surface of various oblique angles. This tape can be attached to common substrates such as glass, polyethylene terephthalate, aluminum sheet, and wood sheet. The corresponding infrared photos show the excellent cooling ability of IREC (Fig. 6(d)). Goods in outdoor transportation and storage often require refrigeration to prevent deterioration or damage from heating up in the sun. For example, the storage facilities of oil tanks, etc., are usually built-in white to prevent stored fuel from being heated to high temperatures by the sun [48–50] (Figs. S19(a) and S19(b) in the ESM). A container from stainless steel is designed to simulate such storage tanks for petroleum, and IREC and different reflective materials are applied to prevent the fuel in the container from heating up in the sunlight. Ethylene glycol is chosen as the measured liquid because

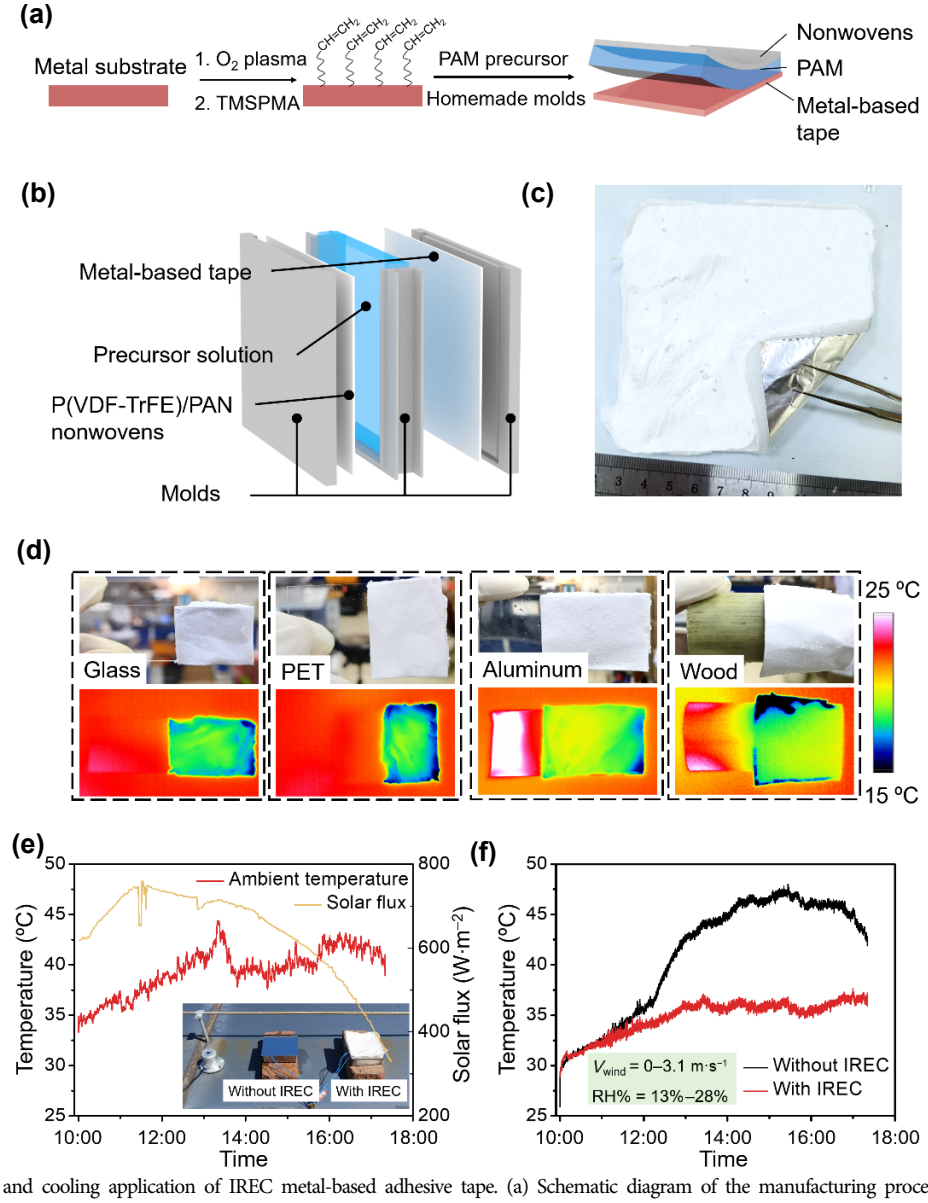

Figure 6 Manufacture and cooling application of IREC metal-based adhesive tape. (a) Schematic diagram of the manufacturing process of IREC metal-based adhesive tapes. By covalently modifying TMSPMA on the surface of the metal tape, cross-linking points can be formed with the hydrogel network. (b) Schematic diagram of using a homemade mold where the nonwovens and metal tape can be clamped on both sides. (c) The photo of a flexible IREC aluminum tape with a size of 10 cm × 10 cm. (d) The photos and the corresponding infrared photos of the IREC aluminum tape pasted on glass, polyethylene terephthalate (PET), aluminum sheet, and wood sheet, respectively. The ambient temperature is 25 °C. (e) Data of solar flux and air temperature during outdoor cooling test. The outdoor experiment was carried out on July 14, 2022 in Beijing. Illustration shows the cooling effect test system for IREC metal-based adhesive tape. (f) Temperature of ethylene glycol in stainless steel containers with and without IREC protection. Wind speed and humidity are marked in the figure.

its specific heat capacity is similar to that of fuel. Three light intensity conditions of 700, 1000, and 1300 W·m^{-2} are used to simulate different weather conditions in outdoor environments. Under irradiation of 1300 W·m^{-2} like a hot summer day, the oil temperature would rise to 43.4 ℃ after 2 h without any reflective coating (Figs. S19(c) and S19(d) in the ESM). A single reflective coating normally employed can reduce the effect of some incident light. The best results are obtained with a porous P(VDF-TrFE) non-woven coating, but the oil temperature still rises to 31.6 ℃. After attaching the IREC aluminum tape to the top stainless steel cover, the temperature of the fuel in the container is maintained at 25 ℃, with almost no temperature rises. Further long-term tests prove that IREC can be operated continuously for more than 16 h and is easily regenerated (Fig. S20 in the ESM), which is sufficient for prolonged daytime use. Compared with other reflective coatings, the IREC cover not only avoids the temperature increase in the container under strong light, but even has the effect of reducing the oil by 0.7 ℃ under low solar flux of 700 W·m^{-2}. Further verification of the cooling effect of IREC on the stored items in containers in an outdoor environment was carried out on July 14, 2022, Beijing (Fig. 6(e)). The solar flux ranges from 600 to 700 W·m^{-2}, while the air temperature ranges from 35 to 42 ℃. The temperature of ethylene glycol in a stainless steel container rises to over 45 ℃ (Fig. 6(f)). In contrast, the temperature of the ethylene glycol with IREC cooling was significantly lower to 36 ℃ and lower than the air temperature. In comparison, the use of IREC can reduce more than 9 ℃ for outdoor storage items, showing great potential in practical cooling applications.

4 Conclusion

An applicable integrated radiative and evaporative cooling technology has been proposed and developed. Highly efficient daytime passive cooling is achieved through the cooperation between strong radiation with visible light reflection and *in situ* evaporation cooling. A record-high cooling power of 710 W·m^{-2} is realized, and the outdoor cooling power with water body storage reaches 630 W·m^{-2}. Further, IREC offers a wealth of utility in both personal cooling management and industrial assisted cooling applications. The IREC-based cooling patch can assist in cooling human body by 13 ℃ for more than 12 h. It can also maintain the temperature of industrial storage facilities such as oil tanks at room temperature under strong sunlight, preventing goods from deteriorating under the influence of high temperatures. This work makes a breakthrough over daytime passive cooling limit by combining radiative and evaporative cooling, which provides a feasible solution for facile, scalable, and affordable long-term efficient passive cooling.

Acknowledgements

This work was supported by the financial support from National Natural Science Foundation of China (Nos. 52073159, 22035005, 52022051, 22075165, and 52090030), State Key Laboratory of Tribology (No. SKLT2021B03), Tsinghua-Foshan Innovation Special Fund (No. 2018THFS0412). This work is also supported by a grant (No. 2019GQG1025) from the Institute for Guo Qiang, Tsinghua University.

Electronic Supplementary Material: Supplementary material (additional optical image, SEM image, cooling performance characterization and analysis) is available in the online version of this article at https://doi.org/10.26599/NRE.2023.9120060.

Declaration of conflicting interests

The authors declare no conflicting interests regarding the content of this article.

References

[1] Omer, A. M. Energy, environment and sustainable development. *Renew. Sust. Energy Rev.* **2008**, *12*, 2265–2300.
[2] Santamouris, M. Cooling the cities—A review of reflective and green roof mitigation technologies to fight heat island and improve comfort in urban environments. *Solar Energy* **2014**, *103*, 682–703.
[3] Zhao, H. X.; Magoulès, F. A review on the prediction of building energy consumption. *Renew. Sust. Energy Rev.* **2012**, *16*, 3586–3592.
[4] Santamouris, M.; Synnefa, A.; Karlessi, T. Using advanced cool materials in the urban built environment to mitigate heat islands and improve thermal comfort conditions. *Solar Energy* **2011**, *85*, 3085–3102.
[5] Raman, A. P.; Anoma, M. A.; Zhu, L. X.; Rephaeli, E.; Fan, S. H. Passive radiative cooling below ambient air temperature under direct sunlight. *Nature* **2014**, *515*, 540–544.
[6] Chen, Z.; Zhu, L. X.; Raman, A.; Fan, S. H. Radiative cooling to deep sub-freezing temperatures through a 24-h day-night cycle. *Nat. Commun.* **2016**, *7*, 13729.
[7] Li, T.; Zhai, Y.; He, S. M.; Gan, W. T.; Wei, Z. Y.; Heidarinejad, M.; Dalgo, D.; Mi, R. Y.; Zhao, X. P.; Song, J. W. et al. A radiative cooling structural material. *Science* **2019**, *364*, 760–763.
[8] Song, J.; Zhang, W.; Sun, Z.; Pan, M.; Tian, F.; Li, X.; Ye, M.; Deng, X. Durable radiative cooling against environmental aging. *Nat. Commun.* **2022**, *13*, 4805.
[9] Zhai, Y.; Ma, Y. G.; David, S. N.; Zhao, D. L.; Lou, R. N.; Tan, G.; Yang, R. G.; Yin, X. B. Scalable-manufactured randomized glass-polymer hybrid metamaterial for daytime radiative cooling. *Science* **2017**, *355*, 1062–1066.
[10] Zhao, B.; Hu, M. K.; Ao, X. Z.; Chen, N.; Pei, G. Radiative cooling: A review of fundamentals, materials, applications, and prospects. *Appl. Energy* **2019**, *236*, 489–513.
[11] Zhu, L. X.; Raman, A. P.; Fan, S. H. Radiative cooling of solar absorbers using a visibly transparent photonic crystal thermal blackbody. *Proc. Natl. Acad. Sci. USA* **2015**, *112*, 12282–12287.
[12] Mandal, J.; Fu, Y. K.; Overvig, A.; Jia, M. X.; Sun, K. R.; Shi, N. N.; Zhou, H.; Xiao, X. H.; Yu, N. F.; Yang, Y. Hierarchically porous polymer coatings for highly efficient passive daytime radiative cooling. *Science* **2018**, *362*, 315–319.
[13] Peng, Y. C.; Chen, J.; Song, A. Y.; Catrysse, P. B.; Hsu, P. C.; Cai, L. L.; Liu, B. F.; Zhu, Y. Y.; Zhou, G. M.; Wu, D. S. et al. Nanoporous polyethylene microfibres for large-scale radiative cooling fabric. *Nat. Sustain.* **2018**, *1*, 105–112.
[14] Li, D.; Liu, X.; Li, W.; Lin, Z. H.; Zhu, B.; Li, Z. Z.; Li, J. L.; Li, B.; Fan, S. H.; Xie, J. W. et al. Scalable and hierarchically designed polymer film as a selective thermal emitter for high-performance all-day radiative cooling. *Nat. Nanotechnol.* **2021**, *16*, 153–158.
[15] Zhou, L. ; Zhao, J. T. ; Huang, H. Y. ; Nan, F. ; Zhou, G. H. ; Ou, Q. D. Flexible polymer photonic films with embedded microvoids for high-performance passive daytime radiative cooling. *ACS Photonics* **2021**, *8*, 3301–3307.
[16] Wang, T. ; Wu, Y. ; Shi, L. ; Hu, X. H. ; Chen, M. ; Wu, L. M. A structural polymer for highly efficient all-day passive radiative cooling. *Nat. Commun* **2021**, *12*, 365.
[17] Aili, A.; Yin, X. B.; Yang, R. G. Passive sub-ambient cooling: Radiative cooling versus evaporative cooling. *Appl. Therm. Eng.* **2022**, *202*, 117909.
[18] Yin, X. B.; Yang, R. G.; Tan, G.; Fan, S. H. Terrestrial radiative cooling: Using the cold universe as a renewable and sustainable energy source. *Science* **2020**, *370*, 786–791.
[19] Zhao, D. L.; Aili, A.; Zhai, Y.; Xu, S. Y.; Tan, G.; Yin, X. B.; Yang, R. G. Radiative sky cooling: Fundamental principles, materials, and applications. *Appl. Phys. Rev.* **2019**, *6*, 021306.

[20] Feng, C. Z.; Yang, P. H.; Liu, H. D.; Mao, M. R.; Liu, Y. P.; Xue, T.; Fu, J.; Cheng, T.; Hu, X. J.; Fan, H. J. et al. Bilayer porous polymer for efficient passive building cooling. *Nano Energy* **2021**, *85*, 105971.
[21] Li, J. L.; Wang, X. Y.; Liang, D.; Xu, N.; Zhu, B.; Li, W.; Yao, P. C.; Jiang, Y.; Min, X. Z.; Huang, Z. Z. et al. A tandem radiative/evaporative cooler for weather-insensitive and high-performance daytime passive cooling. *Sci. Adv.* **2022**, *8*, eabq0411.
[22] Goldstein, E. A.; Raman, A. P.; Fan, S. H. Sub-ambient non-evaporative fluid cooling with the sky. *Nat. Energy* **2017**, *2*, 17143.
[23] Zhao, D. L.; Aili, A.; Zhai, Y.; Lu, J. T.; Kidd, D.; Tan, G.; Yin, X. B.; Yang, R. G. Subambient cooling of water: Toward real-world applications of daytime radiative cooling. *Joule* **2019**, *3*, 111–123.
[24] Yuan, J. C.; Yin, H. L.; Cao, P.; Yuan, D.; Xu, S. Y. Daytime radiative cooling of enclosed water using spectral selective metamaterial based cooling surfaces. *Energy Sustain. Dev.* **2020**, *57*, 22–31.
[25] Aili, A.; Zhao, D. L.; Lu, J. T.; Zhai, Y.; Yin, X. B.; Tan, G.; Yang, R. G. A kW-scale, 24-hour continuously operational, radiative sky cooling system: Experimental demonstration and predictive modeling. *Energy Convers. Manage.* **2019**, *186*, 586–596.
[26] Eicker, U.; Dalibard, A. Photovoltaic-thermal collectors for night radiative cooling of buildings. *Solar Energy* **2011**, *85*, 1322–1335.
[27] Hu, M. K.; Zhao, B.; Suhendri, S.; Cao, J. Y.; Wang, Q. L.; Riffat, S.; Yang, R. G.; Su, Y. H.; Pei, G. Experimental study on a hybrid solar photothermic and radiative cooling collector equipped with a rotatable absorber/emitter plate. *Appl. Energy* **2022**, *306*, 118096.
[28] Li, W. C.; Liu, X. B.; Deng, Z. S.; Chen, Y. T.; Yu, Q. Q.; Tang, W.; Sun, T. L.; Zhang, Y. S.; Yue, K. Tough bonding, on-demand debonding, and facile rebonding between hydrogels and diverse metal surfaces. *Adv. Mater.* **2019**, *31*, 1904732.
[29] Yuk, H.; Zhang, T.; Lin, S. T.; Parada, G. A.; Zhao, X. H. Tough bonding of hydrogels to diverse non-porous surfaces. *Nat. Mater.* **2016**, *15*, 190–196.
[30] van de Hulst, H. C. *Light Scattering by Small Particles*; Wiley: New York, 1957.
[31] Kerker, M. *The Scattering of Light and Other Electromagnetic Radiation*; Academic Press: Cambridge, 1969.
[32] Yao, H. Z.; Zhang, P. P.; Huang, Y. X.; Cheng, H. H.; Li, C.; Qu, L. T. Highly efficient clean water production from contaminated air with a wide humidity range. *Adv. Mater.* **2020**, *32*, 1905875.
[33] Yao, H. Z.; Zhang, P. P.; Yang, C.; Liao, Q. H.; Hao, X. Z.; Huang, Y. X.; Zhang, M.; Wang, X. B.; Lin, T. Y.; Cheng, H. H. et al. Janus-interface engineering boosting solar steam towards high-efficiency water collection. *Energy Environ. Sci.* **2021**, *14*, 5330–5338.
[34] Zhang, P. P.; Liao, Q. H.; Yao, H. Z.; Cheng, H. H.; Huang, Y. X.; Yang, C.; Jiang, L.; Qu, L. T. Three-dimensional water evaporation on a macroporous vertically aligned graphene pillar array under one sun. *J. Mater. Chem. A* **2018**, *6*, 15303–15309.
[35] Zhang, P. P.; Liu, F.; Liao, Q. H.; Yao, H. Z.; Geng, H. Y.; Cheng, H. H.; Li, C.; Qu, L. T. A microstructured graphene/poly(*N*-isopropylacrylamide) membrane for intelligent solar water evaporation. *Angew. Chem., Int. Ed.* **2018**, *57*, 16343–16347.
[36] Zhang, P. P.; Liao, Q. H.; Yao, H. Z.; Huang, Y. X.; Cheng, H. H.; Qu, L. T. Direct solar steam generation system for clean water production. *Energy Stor. Mater.* **2019**, *18*, 429–446.
[37] Wei, Z. C.; Wang, J.; Guo, S.; Tan, S. C. Towards highly salt-rejecting solar interfacial evaporation: Photothermal materials selection, structural designs, and energy management. *Nano Res. Energy* **2022**, *1*, 9120014.
[38] Wong, R. Y. M.; Tso, C. Y.; Chao, C. Y. H. Thermo-radiative energy conversion efficiency of a passive radiative fluid cooling system. *Renew. Energy* **2021**, *180*, 700–711.
[39] Wang, H.; Zhang, R. J.; Yuan, D.; Xu, S. Y.; Wang, L. Y. Gas foaming guided fabrication of 3D porous plasmonic nanoplatform with broadband absorption, tunable shape, excellent stability, and high photothermal efficiency for solar water purification. *Adv. Funct. Mater.* **2020**, *30*, 2003995.
[40] Zhao, F.; Zhou, X. Y.; Shi, Y.; Qian, X.; Alexander, M.; Zhao, X. P.; Mendez, S.; Yang, R. G.; Qu, L. T.; Yu, G. H. Highly efficient solar vapour generation via hierarchically nanostructured gels. *Nat. Nanotechnol.* **2018**, *13*, 489–495.
[41] Li, X. Y.; Peoples, J.; Yao, P. Y.; Ruan, X. L. Ultrawhite $BaSO_4$ paints and films for remarkable daytime subambient radiative cooling. *ACS Appl. Mater. Interfaces* **2021**, *13*, 21733–21739.
[42] Dai, B.; Li, K.; Shi, L. X.; Wan, X. Z.; Liu, X.; Zhang, F. L.; Jiang, L.; Wang, S. T. Bioinspired janus textile with conical micropores for human body moisture and thermal management. *Adv. Mater.* **2019**, *31*, 1904113.
[43] Guan, M. H.; Annaheim, S.; Li, J.; Camenzind, M.; Psikuta, A.; Rossi, R. M. Apparent evaporative cooling efficiency in clothing with continuous perspiration: A sweating manikin study. *Int. J. Therm. Sci.* **2019**, *137*, 446–455.
[44] Peng, Y. C.; Li, W.; Liu, B. F.; Jin, W. L.; Schaadt, J.; Tang, J.; Zhou, G. M.; Wang, G. Y.; Zhou, J. W.; Zhang, C. et al. Integrated cooling (i-Cool) textile of heat conduction and sweat transportation for personal perspiration management. *Nat. Commun.* **2021**, *12*, 6122.
[45] Havenith, G.; Bröde, P.; den Hartog, E.; Kuklane, K.; Holmer, I.; Rossi, R. M.; Richards, M.; Farnworth, B.; Wang, X. X. Evaporative cooling: Effective latent heat of evaporation in relation to evaporation distance from the skin. *J. Appl. Physiol.* **2013**, *114*, 778–785.
[46] Katić, K.; Li, R. L.; Zeiler, W. Thermophysiological models and their applications: A review. *Build. Environ.* **2016**, *106*, 286–300.
[47] Torii, M. Maximal sweating rate in humans. *J. Human Ergol.* **1995**, *24*, 137–152.
[48] Farzaneh-Gord, M.; Nabati, A.; Niazmand, H. Solar radiation effects on evaporative losses of floating roof storage tanks. *Int. J. Oil Gas Coal Technol.* **2011**, *4*, 134–155.
[49] Song, Z. N.; Zhang, W. D.; Shi, Y. X.; Song, J. R.; Qu, J.; Qin, J.; Zhang, T.; Li, Y. W.; Zhang, H. Q.; Zhang, R. P. Optical properties across the solar spectrum and indoor thermal performance of cool white coatings for building energy efficiency. *Energy Build.* **2013**, *63*, 49–58.
[50] Zhang, W. D.; Song, Z. N.; Song, J. R.; Shi, Y. X.; Qu, J.; Qin, J.; Zhang, T.; Li, Y. W.; Zhang, H. Q.; Zhang, R. P. A systematic laboratory study on an anticorrosive cool coating of oil storage tanks for evaporation loss control and energy conservation. *Energy* **2013**, *58*, 617–627.

Houze Yao received his Bachelor's degree in Chemistry from Tsinghua University in 2018. He is currently a Ph.D. candidate at Department of Mechanical Engineering in Tsinghua University. His researches mainly focus on the polymer-based materials, applications on solar energy conversion and environmental protection.

Prof. Liangti Qu received a Ph.D. in Chemistry from Tsinghua University in 2004. He is currently Changjiang Professor at Department of Chemistry in Tsinghua University. His research interests lie in materials chemistry about the synthesis, functionalization and energy-related applications of nanomaterials with carbon–carbon conjugated structures.